



ALMA MATER STUDIORUM
UNIVERSITÀ DI BOLOGNA

ARCHIVIO ISTITUZIONALE
DELLA RICERCA

Alma Mater Studiorum Università di Bologna Archivio istituzionale della ricerca

Extended dynamic mode decomposition for model reduction in fluid dynamics simulations

This is the final peer-reviewed author's accepted manuscript (postprint) of the following publication:

Published Version:

Libero, G., Chiofalo, A., Ciriello, V., Tartakovsky, D.M. (2024). Extended dynamic mode decomposition for model reduction in fluid dynamics simulations. PHYSICS OF FLUIDS, 36(6), 1-10 [10.1063/5.0207957].

Availability:

This version is available at: <https://hdl.handle.net/11585/975236> since: 2024-07-22

Published:

DOI: <http://doi.org/10.1063/5.0207957>

Terms of use:

Some rights reserved. The terms and conditions for the reuse of this version of the manuscript are specified in the publishing policy. For all terms of use and more information see the publisher's website.

This item was downloaded from IRIS Università di Bologna (<https://cris.unibo.it/>).
When citing, please refer to the published version.

(Article begins on next page)

This is the author's peer reviewed, accepted manuscript. However, the online version of record will be different from this version once it has been copyedited and typeset.

PLEASE CITE THIS ARTICLE AS DOI: 10.1063/5.0207957

1 **Extended dynamic mode decomposition for model reduction in fluid dynamics**
 2 **simulations**

3 Giulia Libero,¹ Alessia Chiofalo,¹ Valentina Ciriello,¹ and Daniel M. Tartakovsky^{2, a)}

4 ¹⁾*Department of Civil, Chemical, Environmental and Materials Engineering,*
 5 *University of Bologna, via Zamboni, 33-40126 Bologna,*
 6 *Italy*

7 ²⁾*Department of Energy Science and Engineering, Stanford University,*
 8 *367 Panama St., Stanford, CA 94305, USA*

9 (Dated: 30 May 2024)

10 High computational cost and storage/memory requirements of fluid dynamics simu-
 11 lations constrain their usefulness as a predictive tool. Reduced-order models (ROMs)
 12 provide a viable solution to this challenge by extracting the key underlying dynamics
 13 of a complex system directly from data. We investigate the efficacy and robustness of
 14 an extended dynamic mode decomposition (xDMD) algorithm in constructing ROMs
 15 of three-dimensional cardiovascular computations. Focusing on the ROMs' accuracy
 16 in representation and interpolation, we relate these metrics to the truncation rank
 17 of singular value decomposition, which underpins xDMD and other approaches to
 18 ROM construction. Our key innovation is to relate the truncation rank to the sin-
 19 gular values of the original flow problem. This result establishes a priori guidelines
 20 for the xDMD deployment and its likely success as a means of data compression and
 21 reconstruction of the system's dynamics from dominant spatiotemporal structures
 22 present in the data.

^{a)}tartakovsky@stanford.edu

23 I. INTRODUCTION

24 High computational burden of fluid dynamics simulations has propelled the develop-
 25 ment of model reduction techniques for problems dealing with complex flow and transport
 26 processes in fields as diverse as geosciences and biomedicine¹⁻⁵. A reduced-order model
 27 (ROM) is a computationally efficient and reasonably accurate representation of the underly-
 28 ing dynamics of a state variable or a quantity of interest, derived from observations and/or
 29 computer-generated data. The efficiency of a model reduction technique manifests itself in
 30 both the amount of data required for the ROM construction and the ROM approximation
 31 accuracy in the interpolation and extrapolation regimes⁶.

32 Dynamic mode decomposition (DMD) is a data-driven technique that constructs ROMs of
 33 complex dynamical systems by employing the singular value decomposition (SVD)^{7,8}. DMD
 34 aims to identify spatiotemporal structures that are dominant in the data and to reconstruct
 35 an optimal linear model from these structures. A DMD variant xDMD⁹ combines salient
 36 features of the residual learning¹⁰ and the generalized DMD with a bias term¹¹. This DMD
 37 algorithm has the ability to handle dynamical systems described by inhomogeneous partial
 38 differential equations, which proved to be problematic for standard DMD. Numerical studies,
 39 dealing with problems as diverse as the Navier-Stokes equations⁹ and multiphase transport in
 40 porous media¹², suggest that the xDMD is more accurate than the standard DMD algorithm
 41 (hereinafter, sDMD¹³). Since xDMD has more parameters than sDMD (the bias term), it is
 42 potentially more sensitive to noise than. However, the numerical experiments⁹ indicate that
 43 the correction effects from the bias term may dominate the effects of over-fitting the noise.

44 These and other methods for ROM construction rely on the truncation rank of SVD
 45 to control the degree of order reduction and representation accuracy. The choice of how
 46 many singular values to keep depends on such factors as the quality and origin of the data
 47 and the dynamic importance of low-energy modes¹³. The rank selection is typically done
 48 via experimentation, rendering the method's implementation subjective. A more principled
 49 approach is to balance order reduction and approximation accuracy by utilizing a general
 50 criteria¹². The rank choice is also linked to xDMD's data compression ability, which is given
 51 by the capability of the algorithm to preserve high accuracy for low values of the truncation
 52 rank^{12,13}. By identifying dominant coherent structures from data, the method effectively
 53 reduces the dimensionality of high-dimensional datasets, thereby achieving compression-like

This is the author's peer reviewed, accepted manuscript. However, the online version of record will be different from this version once it has been copyedited and typeset.

PLEASE CITE THIS ARTICLE AS DOI: 10.1063/1.50207957

54 effects. That is relevant in fluid dynamics, where DMD operates by reducing the dimension-
 55 ality of the flow field data while preserving its essential characteristics. Another application
 56 is climate science, where DMD can be used to compress large-scale climate datasets into a
 57 reduced set of dominant modes, facilitating the analysis and visualization of long-term cli-
 58 mate trends and variability¹³. In yet another setting of multiphase flow in porous media¹²,
 59 xDMD demonstrated high prediction accuracy (relative interpolation error on the order of
 60 10^{-9}) with a truncation rank of up to 35% of the dataset dimension. By way of a disclaimer,
 61 we note that, like other SVD-based techniques, DMD often struggles to honor translational
 62 and rotational invariances of low-rank objects embedded in the data¹³.

63 Our study has three intertwined goals. The first is to analyze how the representation
 64 error of xDMD is affected by the truncation rank in SVD, which, in turn, is linked to
 65 singular values of the problem. The second is to test the xDMD-based ROM in terms
 66 of its interpolation error, for different truncation ranks. The third goal is to explore the
 67 effect of neglecting possible irrelevant/overfit-inducing information (noise) on the accuracy
 68 of the approximation. We pursue these goals in the context of three-dimensional (3D)
 69 cardiovascular simulations of blood flow in a complex geometry of a patient-specific aorta.

70 The reference aorta geometry is selected from the Vascular Model Repository (www.
 71 vascularmodel.com), a library of patient-specific cardiovascular models developed on volu-
 72 metric image data sets and relevant physiologic data¹⁴. Fluid dynamics data are generated
 73 with **SimVascular** (<http://simvascular.github.io/>). The latter is an open-source software
 74 that provides a complete pipeline, from medical image data segmentation to patient-specific
 75 blood flow simulations based on the 3D incompressible Navier-Stokes equations¹⁵. We use
 76 a data set consisting of $\approx 2 \cdot 10^3$ time frames of the velocity distribution (on a mesh with
 77 $\sim 10^5$ elements) in a selected aorta.

78 Our research provides practical guidelines for the selection of low-rank truncation options
 79 for optimal order-reduction (data compression). Our findings suggest that excluding low-
 80 energy modes, which do not contribute to the elucidation of system dynamics, is beneficial
 81 to ROM accuracy. We also found the ROM accuracy to be robust to both the size of time
 82 intervals between the snapshots and low-rank truncations. This conclusion requires a flow
 83 map of the system dynamics to be sufficiently smooth in space. An optimal rank selection
 84 needs to consider the ROM's prediction reliability not only in reproducing the training data
 85 (representation error) but also in making predictions at space-time locations where the data

86 are not available (interpolation error). Once optimized, the ROM can be used to replicate
 87 cardiac function in a low-dimensional space, reducing the simulation cost and facilitating
 88 the optimization and design of patient-specific interventions. At the same time, the DMD-
 89 based modal decomposition allows for the identification of physically interpretable patterns
 90 in the temporal and spatial evolution of the observed cardiovascular phenomena¹⁶. Coherent
 91 structures and dominant flow features can be analyzed to discover the underlying physics
 92 and possibly employed to detect pathologies^{17–21}.

93 The paper is organized as follows: Section II is devoted to the formulation of the problem;
 94 in Section III the xDMD algorithm is described; while in Section IV its application to the
 95 test case is presented and discussed; a set of final remarks in Section V closes the paper.

96 II. PROBLEM FORMULATION

97 Once discretized on a numerical mesh, system states are arranged into a state vector
 98 $\mathbf{u}(t) \in \mathbb{R}^N$ of length N . The temporal evolution of this discretized system is described by a
 99 system of N (nonlinear, homogeneous) ordinary differential equations,

$$100 \quad \frac{d\mathbf{u}}{dt} = \mathbf{f}(\mathbf{u}, \mathbf{s}), \quad \mathbf{u}(0) = \mathbf{u}_0, \quad (1)$$

101 where $\mathbf{f}(\mathbf{u}, \cdot)$ describes the nonlinear dynamics, $\mathbf{s} \in \mathbb{R}^N$ represents the source/sinks term and
 102 boundary conditions, and $\mathbf{u}_0 \in \mathbb{R}^N$ denotes the discretized initial state of the system.

103 Let $\Phi_{\Delta t} : \mathbb{R}^N \rightarrow \mathbb{R}^N$ be a flow map, which relates the discretized system state $\mathbf{u}(t)$ to
 104 $\mathbf{u}(t + \Delta t)$ at any time t and time step Δt .

105 **Lemma 1** *Assume \mathbf{f} is Lipschitz continuous with Lipschitz constant L on a set $\mathcal{H} \subseteq \mathbb{R}^N$.
 106 Define $\mathcal{H}_{\Delta t} = \{\mathbf{y} \in \mathcal{H} : \Phi_{\Delta t}(\mathbf{y}) \in \mathcal{H}\}$. Then, the flow map $\Phi_{\Delta t}$ is Lipschitz continuous on
 107 $\mathcal{H}_{\Delta t}$. Specifically, for any \mathbf{y} and $\tilde{\mathbf{y}} \in \mathcal{H}_{\Delta t}$,*

$$108 \quad \|\Phi_{\Delta t}(\mathbf{y}; \mathbf{s}) - \Phi_{\Delta t}(\tilde{\mathbf{y}}; \mathbf{s})\| \leq e^{L\tau} \|\mathbf{y} - \tilde{\mathbf{y}}\|, \forall \tau \in [t, t + \Delta t].$$

109 The proof follows from the classical result on the continuity of a dynamical system (p. 109
 110 in Ref. 22). The local Lipschitz continuity of the flow map ensures that nearby tra-
 111 jectories evolve smoothly and predictably, which is critical for the validity of the DMD
 112 approximation¹¹. Moreover, if the flow map is locally Lipschitz continuous, the system's
 113 behavior can be accurately represented by a finite number of modes that evolve smoothly

114 in time, thus aiding interpretation and forecasting. Various DMD studies²³ indicate that a
115 linear operator might not be a good approximation of the general flow map, particularly for
116 highly nonlinear problems. In such cases, it might be necessary to map the state variables
117 onto observables¹³.

118 The DMD approach approximates the nonlinear dynamical system, i.e., $\mathbf{f}(\mathbf{u}, \cdot)$, with
119 a linear model constructed from M temporal snapshots of the discretized state variable,
120 $\mathbf{x}_k = \mathbf{u}(t_k)$ with $k = 0, \dots, M - 1$. In general, numerical simulations involve discretizing
121 continuous processes into time steps. The continuous nature of the flow map enables in-
122 terpolation between simulation time steps or extrapolation beyond them, providing a more
123 precise representation of the system's behavior.

124 Let \mathcal{L} be a DMD-based ROM of the dynamical system (1). At time t_k , the true solution
125 induced by the flow map $\Phi_{\Delta t}$ and its DMD approximation are

$$126 \quad \mathbf{x}_k = \Phi_{\Delta t}(\mathbf{x}_{k-1}) \quad \text{and} \quad \mathbf{x}_k^{\mathcal{L}} = \mathcal{L}(\mathbf{x}_{k-1}^{\mathcal{L}}), \quad (2)$$

127 respectively. The error of a DMD model at time t_k is

$$128 \quad \delta_k^{\mathcal{L}} = \|\mathbf{x}_k^{\mathcal{L}} - \mathbf{x}_k\|, \quad (3)$$

129 where $\|\cdot\|$ denotes vector 2-norm. The error bounds for xDMD and sDMD, reported in
130 Appendix A, provide a general indicator⁹ for the growth of $\delta_k^{\mathcal{L}}$. The numerical experiments
131 reported in Section IV serve to investigate this error in detail.

132 III. THE XDMD ALGORITHM

133 Consider a set of $(M+1)$ snapshots of the vector of state variables, \mathbf{x}_k with $t_{k+1} = t_k + \Delta t$ and
134 $k = 0, \dots, M$. Let $\mathbf{X} \in \mathbb{R}^{N \times M}$ denote a matrix whose columns are the vectors $\mathbf{x}_0, \dots, \mathbf{x}_{M-1}$.
135 Let $\mathbf{X}' \in \mathbb{R}^{N \times M}$ denote a matrix whose columns are the vectors $\mathbf{x}_1, \dots, \mathbf{x}_M$. The sDMD
136 algorithm describes the temporal evolution of $\mathbf{u}(t)$ with a linear model

$$137 \quad \mathbf{x}_{k+1} \approx \mathbf{A}\mathbf{x}_k, \quad \mathbf{A} = \mathbf{X}'\mathbf{X}^\dagger \in \mathbb{R}^{N \times N}. \quad (4)$$

138 In a typical application, $M \ll N$ so that the rank of \mathbf{A} is at most M . Even though,
139 computing \mathbf{A} (or its spectral decomposition) is generally onerous. Instead, the truncated
140 SVD of $\mathbf{X} = \mathbf{U}\Sigma\mathbf{V}^\top$, with rank $r < M$, is used¹³:

$$141 \quad \mathbf{A} \approx \mathbf{X}'\mathbf{V}\Sigma^{-1}\mathbf{U}^\top, \quad (5)$$

142 where $\mathbf{U} \in \mathbb{R}^{N \times r}$, $\mathbf{\Sigma} \in \mathbb{R}^{r \times r}$, $\mathbf{V} \in \mathbb{R}^{M \times r}$. If r is smaller than the number of nonzero singular
 143 values (i.e., the rank of \mathbf{X}), then the truncated SVD is a proxy of \mathbf{X} .

144 To allow for a problem's inhomogeneity, the generalized DMD algorithm adds a bias term
 145 $\mathbf{b}_g \in \mathbb{R}^N$ to the standard formulation,

$$146 \quad \mathbf{x}_{k+1} \approx \mathbf{A}_g \mathbf{x}_k + \mathbf{b}_g. \quad (6)$$

147 Here, $[\mathbf{A}_g \ \mathbf{b}_g] = \mathbf{X}' \tilde{\mathbf{X}}^\dagger \in \mathbb{R}^{N \times N+1}$, where $\tilde{\mathbf{X}}^\top = [\mathbf{X} \ \mathbf{1}]$ and $\tilde{\mathbf{X}} \in \mathbb{R}^{N+1 \times M}$. The computational
 148 cost is reduced by obtaining the best-fit linear operator through the SVD of the matrix
 149 $\tilde{\mathbf{X}} \approx \mathbf{U}_g \mathbf{\Sigma}_g \mathbf{V}_g^\top$, such that

$$150 \quad [\mathbf{A}_g \ \mathbf{b}_g] \approx \mathbf{X}' \mathbf{V}_g \mathbf{\Sigma}_g^{-1} \mathbf{U}_g^\top, \quad (7)$$

151 where $\mathbf{U}_g \in \mathbb{R}^{N+1 \times r}$, $\mathbf{\Sigma}_g \in \mathbb{R}^{r \times r}$, and $\mathbf{V}_g \in \mathbb{R}^{M \times r}$. By construction, the error of this gDMD
 152 method is equal to or smaller than that of sDMD (Appendix A).

153 The extended DMD (xDMD) approach⁹ endows gDMD with a residual-learning idea. It
 154 approximates the relationship between $\mathbf{Y} = \mathbf{X}' - \mathbf{X}$ and \mathbf{X} ,

$$155 \quad \mathbf{y}_{k+1} = \mathbf{B}_x \mathbf{x}_k + \mathbf{b}_x. \quad (8)$$

156 Here, $[\mathbf{B}_x \ \mathbf{b}_x] = \mathbf{Y} \tilde{\mathbf{X}}^\dagger \in \mathbb{R}^{N \times N+1}$, and $\tilde{\mathbf{X}}^\top \in \mathbb{R}^{N+1 \times M}$ is defined as before. For computational
 157 saving, the best-fit linear operator is obtained through the SVD of the matrix $\tilde{\mathbf{X}}$ as

$$158 \quad [\mathbf{B}_x \ \mathbf{b}_x] \approx \mathbf{Y} \mathbf{V}_g \mathbf{\Sigma}_g^{-1} \mathbf{U}_g^\top. \quad (9)$$

159 The error of xDMD equals to or is smaller than that of the residual DMD without bias
 160 (Appendix A). The impact of the bias term and residual learning on the accuracy of the
 161 DMD method is studied in Ref. 9. An efficient computational strategy to derive prediction
 162 in Eq. (8) is presented in Appendix B.

163 DMD can be used as a ROM of a nonlinear PDE, whose solution is confined in $\mathcal{H} \subseteq \mathbb{R}^N$
 164 (to satisfy the assumptions in Lemma 1). We assess the performance of xDMD, both in
 165 representation and interpolation, in terms of the relative error^{9,12,13}

$$166 \quad \varepsilon_{\mathcal{L}}^k = \frac{\|\mathbf{x}_k^{\mathcal{L}} - \mathbf{x}_k\|^2}{\|\mathbf{x}_k\|^2}, \quad (10)$$

167 where $\|\cdot\|$ denotes vector 2-norm.

168 Several criteria can be used to select the truncation rank of a ROM^{1,12,13}. One is to use
 169 the rank of the data matrix, $r = \text{rank}(\tilde{\mathbf{X}})$, i.e., to incorporate all the information contained

170 in the data, including the noise. Another criterion is based on the cumulative energy in the
 171 SVD of $\tilde{\mathbf{X}}$; for example, one could set $r = r_{90}$, where

$$172 \quad r_{90} = \min(n) : \frac{\sum_{k=0}^n \sigma_k}{\sum_{k=0}^{M-1} \sigma_k} \geq 0.9 \quad (11)$$

173 is the number of diagonal elements of Σ that accounts for 90% of the energy. Yet another
 174 criterion defines $r = r^*$ as the number of diagonal elements of Σ associated with the first
 175 singular value satisfying the inequality

$$176 \quad r^* = \min(n) : \sigma_n \leq 10^{-5} \sum_{k=0}^{M-1} \sigma_k. \quad (12)$$

177 The latter two criteria allow one to ascertain the effect of truncation of low-energy modes,
 178 as we do below.

179 IV. APPLICATION

180 A. 3D Cardiovascular Model

181 We deploy the `SimVascular` software¹⁵ to solve 3D incompressible Navier-Stokes equa-
 182 tions describing blood flow in a patient-specific aorta. A cardiovascular model and the
 183 flow-domain geometry are selected, at random, from the Vascular Model Repository¹⁴; the
 184 homogeneous Dirichlet boundary conditions imposed at the aorta walls imply no-slip veloc-
 185 ity at the rigid wall²⁴. `SimVascular` relies on the 3D Delaunay triangulation to discretize
 186 the flow domain with a triangular mesh of $N = 343352$ elements. (The flow-domain geometry
 187 and the corresponding mesh are available for download from the Vascular Model Reposi-
 188 tory.) A typical 3D finite-element simulations of the unsteady Navier–Stokes of two cardiac
 189 cycles for this type of geometry takes a few hours²⁴. The quantity of interest, arranged in
 190 the vector $\mathbf{u} \in \mathbb{R}^N$ (see Section II), is the velocity magnitude of which $M = 1868$ snapshots,
 191 $\mathbf{u}(t_k)$, are collected over 7.7 s, which covers about 12 pulsations. Columns of matrices \mathbf{X} and
 192 \mathbf{X}' are given by the snapshots of the velocity magnitude computed by `SimVascular` at a
 193 constant time interval (see Section III). We chose the number of snapshots to be sufficiently
 194 large to perform interpolation tests for different time steps.

195 The `SimVascular` predictions are used to perform multiple tests, both in representation
 196 and interpolation regimes, with datasets of reduced (in space and/or time) size to verify the

197 generality of our results. In the representation regime, these tests start with an analysis
 198 of the representation error performed on the entire dataset of $M = 1868$ snapshots, each
 199 consisting of $N = 343352$ grid elements. Next, ROMs are trained on randomly selected
 200 data sets in which N is reduced by a tenth and a hundredth. Finally, ROMs are trained
 201 on randomly selected data sets in which M is reduced to 200 snapshots associated with
 202 different time intervals. In the interpolation-error analysis, we perform several tests for
 203 different interpolation rates. Results and analysis of these tests are presented in the following
 204 section.

205 B. Results and Discussion

206 1. Representation Error and Data Compression

207 We use xDMD to construct ROMs from the entire collection of snapshots of the velocity
 208 magnitude and testing these ROMs' ability to reproduce these training data. This exercise
 209 quantifies the representation error of xDMD. A sequence of ROMs differ from each other
 210 in the truncation rank applied to the SVD. We explore the xDMD accuracy at low-rank
 211 truncations, which are relied upon to identify dominant spatiotemporal structures in the
 212 computer-generated data. This analysis is also relevant for the exploration of xDMD's
 213 effectiveness for data compression and storage.

214 Figure 1a shows the ROMs' representation error, computed with Eq. (10) for different
 215 truncation ranks r and averaged over all the time steps. As expected, the representation
 216 error decreases with the truncation rank r . High accuracy is reached for relatively low r :
 217 when $r = \text{rank}(\tilde{X}) = 1868$, i.e., in the absence of truncation, the representation error is
 218 $3.6 \cdot 10^{-16}$; setting $r = r^* = 357$ or $r = r_{90} = 24$ leads to errors of $2.8 \cdot 10^{-5}$ or $1.5 \cdot 10^{-1}$,
 219 respectively. By considering only 20% of the modes, with $r = r^*$, the result is remarkably
 220 accurate. Additionally, the cumulative energy associated with r^* is approximately equal to
 221 1 (Fig. 1c). That is linked to the rate at which the singular values decrease to 0 (Fig. 1b),
 222 indicating that the limited number of modes captured by r^* are dominant in the dynamics.
 223 The remaining features ($n > 357$) are low-energy modes that do not affect the ROM accuracy;
 224 as such, they can be interpreted as noise and, for the purpose of data compression, can be
 225 neglected.

This is the author's peer reviewed, accepted manuscript. However, the online version of record will be different from this version once it has been copyedited and typeset.

PLEASE CITE THIS ARTICLE AS DOI: 10.1063/1.50207957

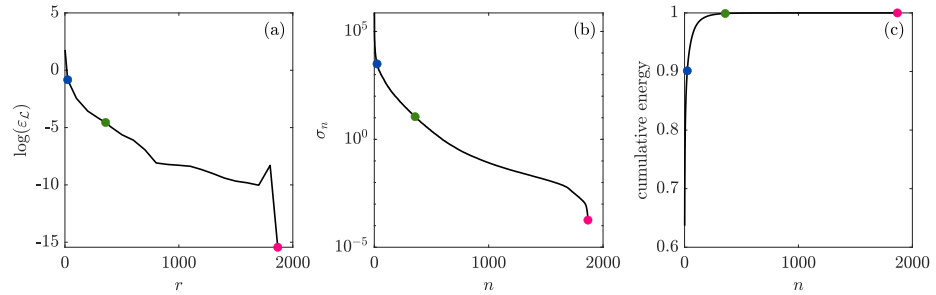


FIG. 1. (a) Representation error (averaged over the time instants) as function of the truncation rank r of the SVD of $\tilde{\mathbf{X}}$ when all data ($N = 343352$, $M = 1868$) are used to train the ROMs. (b) Singular values and (c) cumulative energy associated with the SVD, both plotted as function of the singular values number n . In all panels, the blue, green, and red dots correspond to $r = r_{90}$, $r = r^*$, and $r = \text{rank}(\tilde{\mathbf{X}})$, respectively. In this example, $r_{90} = 24$, $r^* = 357$, and $\text{rank}(\tilde{\mathbf{X}}) = M = 1868$ resulting in no truncation.

226 To elucidate further the effects of the truncation rank on the prediction accuracy of
 227 xDMD, we compare the original data with the corresponding reconstructed snapshots pro-
 228 vided by the ROMs truncated at r_{90} and r^* (Fig. 2). Both ROMs reproduce the general
 229 velocity patterns, although the r_{90} truncation rank returns a slightly worse approximation.
 230 This comparison demonstrates the ROM ability to capture the salient features of the flow,
 231 which suggests that xDMD is suitable for the interpretation and reproduction of 3D car-
 232 diovascular simulations. Depending on the accuracy required by the application, one can
 233 select an appropriate truncation criteria and employ the xDMD-based ROM to replace the
 234 onerous numerical simulations with compressed reconstructions.

235 To test the method's robustness, we train ROMs on data sets with missing spatial data.
 236 Specifically, elements of the original mesh of size N are randomly selected to obtain two
 237 reduced-size data sets of dimensions $N/10$ and $N/100$. Representation accuracy of the
 238 resulting ROMs, trained on all $M = 1868$ temporal snapshots, is shown in Figure 3a, for the
 239 same values of $r = r_{90}$, $r = r^*$, and $r = \text{rank}(\tilde{\mathbf{X}})$. When only the dominant spatiotemporal
 240 structures of the underlying flow are considered, the accuracy close to locations where the
 241 training data are sampled is not affected by the data loss. The error increases with r ,

This is the author's peer reviewed, accepted manuscript. However, the online version of record will be different from this version once it has been copyedited and typeset.

PLEASE CITE THIS ARTICLE AS DOI: 10.1063/1.50207957

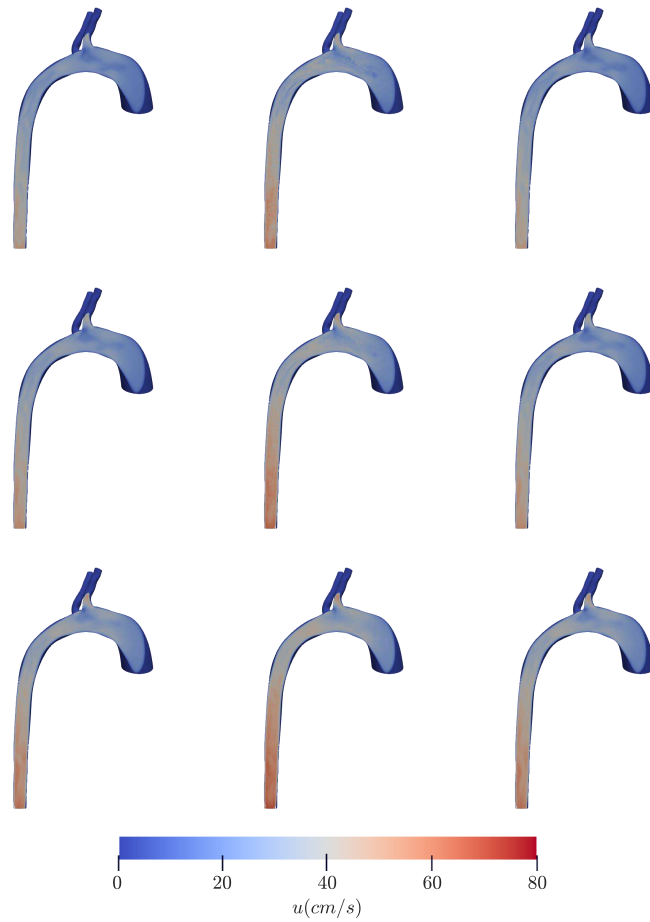


FIG. 2. Magnitude of the flow velocity u in the aorta, as predicted by (left column) direct numerical simulations, (middle column) xDMD with truncation ranks r_{90} , and (right column) xDMD with r^* . The velocity is plotted at times $k = M/3$, $k = 2M/3$ and $k = M$ in the first, second and third rows, respectively.

242 reaching tens of orders of magnitude for $r = \text{rank}(\tilde{\mathbf{X}})$ when all the features contained in the
 243 data are accounted for. This finding suggests that when the data are not sufficiently rich
 244 to cover the solution space of interest, considering low-energy modes does not increase the
 245 ROM accuracy.

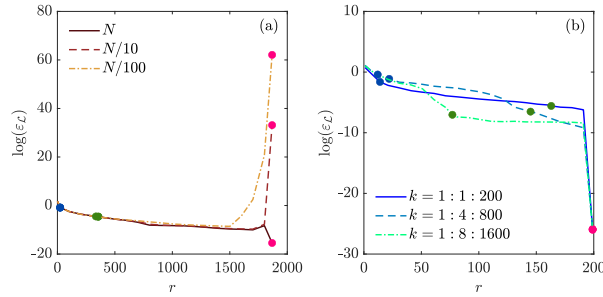


FIG. 3. Dependence of time-averaged representation error of ROMs on the SVD truncation rank r . In (a), the ROMs are alternatively trained on the data in all N pixels and on the data at randomly selected $N/10$ and $N/100$ pixels; in all three cases, using M snapshots. In (b), the ROMs are alternatively trained on the first 200 snapshots and on the 200 snapshots selected with time intervals 4 or 8; in all three cases, using $N/100$ pixels. The blue, green and red dots correspond to $r = r_{90}$, $r = r^*$ and $r = \text{rank}(\tilde{\mathbf{X}})$, respectively.

246 Another facet of xDMD's robustness is its sensitivity to the number of temporal snapshots
 247 available for training. Figure 3b shows the representation error of the xDMD trained on
 248 $N/100$ velocity measurements and 200 snapshots. (These snapshots are selected from the full
 249 data set ($M = 1868$) using either the first 200 images or every fourth or every eighth image.)
 250 This experiment reveals that the ROM's accuracy is not affected by either the reduction of
 251 the number of snapshots or the time step between the snapshots. Hence, xDMD is robust
 252 and provides a good approximation of nonlinear flow phenomena.

253 2. Interpolation Error

254 ROMs are typically employed to make predictions at space-time points wherein the out-
 255 put of fluid dynamic simulations is not available. We test our ROMs' performance in the
 256 interpolation regime for several values of the interpolation rate η . The data-matrix dimen-
 257 sions and truncation ranks for all the cases considered are reported in Table I.

258 We start by constructing three ROMs associated with the truncation rank $r = \text{rank}(\tilde{\mathbf{X}})$,
 259 $r = r^*$ and $r = r_{90}$, and trained on half of the snapshots, i.e., $\eta = 0.5$ (Case 1 in Table I).

TABLE I. Cases considered for interpolation tests.

Case	η	Train set	$r = r_{90}$	$r = r^*$	$\text{rank}(\tilde{\mathbf{X}})$
1	0.5	$k = 1 : 2 : M$	23	252	934
2	0.67	$k = 1 : 3 : M$	23	261	622
3	0.8	$k = 1 : 5 : M$	16	119	373
4	0.9	$k = 1 : 10 : M$	10	62	186

260 Interpolation errors of these ROMs are shown in Figure 4a; the errors are defined in Eq. (10)
 261 and predictions are carried out for the missing half of time steps. The ROM truncated at
 262 $r = r^*$ assures high accuracy and stability (the error varies between 10^{-5} and 10^{-4} at all
 263 times), while the truncation at $r = \text{rank}(\tilde{\mathbf{X}})$ results in the error that increases with time;
 264 if $r = r_{90}$ the error is stable in time but about three orders of magnitude higher than in
 265 the case of $r = r^*$ (it varies between 10^{-2} and $10^{-0.5}$). Reducing the size of the training
 266 set, i.e., setting $\eta = 0.67$ (Case 2 in Table I), yields the two different ROMs truncated at r^*
 267 and $\text{rank}(\tilde{\mathbf{X}})$ with similar interpolation errors, while $r = r_{90}$ produces a significantly higher
 268 error (Figure 4b); for all r considered, the respective ROMs' error peaks are aligned and
 269 the periodicity is similar, with $r = r^*$ providing a smaller error. In the cases of $\eta = 0.8$ and
 270 $\eta = 0.9$ (Cases 3 and 4 in Table I, respectively) the interpolation errors of all the ROMs
 271 increase with time and the difference when truncating at r^* and $\text{rank}(\tilde{\mathbf{X}})$ relative to $r = r_{90}$
 272 decreases till about one order of magnitude in the case of $\eta = 0.9$ (Figure 4c-d).

273 To provide a local view on the ROMs' accuracy, Figure 5 compares the reference and
 274 reconstructed velocity time series at two points in a cross-section of the aorta for Cases 3
 275 and 4 in Table I in panels (a) and (c) and (b) and (d), respectively. As expected, the ROM
 276 truncated at rank $r = r^*$ (panels (c) and (d)) has high accuracy both in representation and
 277 interpolation for all the points considered; instead, the ROM truncated at $r = r_{90}$ (panels
 278 (a) and (b)) fails to adequately reproduce the overall system state and loses accuracy when
 279 η or t increases. The ROM's performance is not affected by the selection of the points near
 280 the wall or in the middle of the aorta.

281 These results provide actionable indicators for the rank choice and the role played by the
 282 non-dominant modes. When all the modes are included in the training phase, $r = \text{rank}(\tilde{\mathbf{X}})$,

This is the author's peer reviewed, accepted manuscript. However, the online version of record will be different from this version once it has been copyedited and typeset.

PLEASE CITE THIS ARTICLE AS DOI: 10.1063/1.50207957

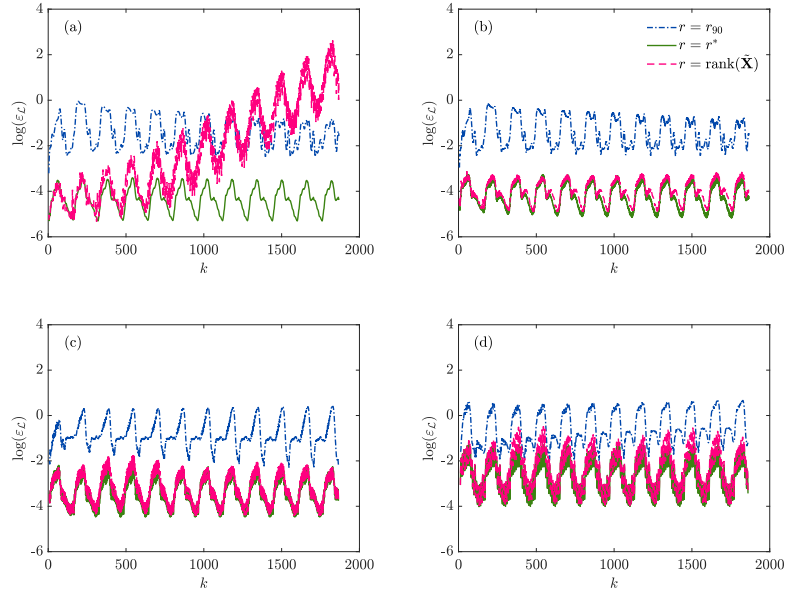


FIG. 4. Interpolation errors for (a) Case 1, (b) Case 2, (c) Case 3, and (d) Case 4 in Table I. In each plot different lines correspond to the ROMs with different truncation ranks $r = r_{90}$, $r = r^*$ and $r = \text{rank}(\bar{\mathbf{X}})$.

283 the ROM suffers from noise overfitting and loses its interpolation accuracy, especially when
 284 the training set is larger ($\eta = 0.5$). The loss in accuracy is difficult to predict given the
 285 lack of a priori error estimators. Hence, the use of a low-rank truncation not only aligns
 286 with a ROM's purpose (identification of the dominant modes and data compression) but
 287 also increases the ROM's prediction reliability at space-time locations where data are not
 288 available.

289 V. CONCLUSION

290 We analyzed the performance of an extended dynamic mode decomposition (xDMD)⁹ on
 291 the task of ROM construction to approximate the fluid dynamics simulations of 3D blood

This is the author's peer reviewed, accepted manuscript. However, the online version of record will be different from this version once it has been copyedited and typeset.

PLEASE CITE THIS ARTICLE AS DOI: 10.1063/1.5207957

308 compression, which is beneficial in many fields, but also allows us to reconstruct the sys-
 309 tem's behavior where data is unavailable (in interpolation or extrapolation regimes) with a
 310 single linear model providing predictions everywhere in space at any given time. This linear
 311 model is readily interpretable and is cleansed of noise, which would otherwise impede the
 312 reconstruction.

313 Our study demonstrates that the identification of an optimal DMD structure requires
 314 the selection of a low-rank approximation able to guarantee the ROM's accuracy in both
 315 representation and interpolation. This instill trust in the ROM's predictions, paving the way
 316 for their use in clinical practice. For example, DMD can be employed to predict blood flow
 317 beyond the available data to study variations in the flow waveform¹⁷, to provide reliable
 318 real-time forecasting of tumor ablation treatment²⁵, and to facilitate spectral analysis in
 319 dynamic MRI acquisitions to advance the diagnostic potential²⁰.

320 Since DMD is formulated entirely in terms of (observational and/or simulated) data, it
 321 can be readily deployed in a wide range of applications, including in real-time simulation
 322 environments. In this context, newly available data can be absorbed in the training phase
 323 while updating the future state prediction.

324 ACKNOWLEDGMENTS

325 The authors would like to acknowledge Alison Marsden and Luca Pegolotti for providing
 326 the HFM data. The data that support the findings of this study are openly available in the
 327 repository www.vascularmodel.com.¹⁴ This study has received funding from the Research
 328 Project of National Interest PRIN 2017 "Fluid dynamics of hearts at risk of failure: to-
 329 wards methods for the prediction of disease progression", funded by the Italian Ministry of
 330 Education, Universities and Research (MIUR); MIUR code: 2017A889FP.006; CUP code:
 331 J34I19001480001. GL has also received funding from the Marco Polo mobility scholarship
 332 for research 2021 of the University of Bologna. DMT was funded, in part, by the Air Force
 333 Office of Scientific Research under grant FA9550-21-1-0381, by the Office of Advanced Sci-
 334 entific Computing Research (ASCR) within the Department of Energy Office of Science
 335 under award number DE-SC0023163, and by the Strategic Environmental Research and
 336 Development Program (SERDP) of the Department of Defense under award RC22-3278.

337 Appendix A: Error bounds

338 In addition to the assumptions in Lemma 1, we assume that $\|\mathcal{L} - \Phi_{\Delta t}\|_{L^\infty(\mathcal{H}_{\Delta t})} < +\infty$ and
 339 that \mathbf{x}_k and $\mathbf{x}_k^{\mathcal{L}} \in \mathcal{H}_{\Delta t}$ for $k = 0, \dots, M - 1$. If \mathcal{L} is sDMD, then the error $\delta_{\mathcal{L}}^M$ at time t_M ,
 340 defined in (3), satisfies the inequality

$$341 \quad \delta_{\mathcal{L}}^M \leq e^{ML\Delta t} \delta_{\mathcal{L}}^0 + \|\mathcal{L} - \Phi_{\Delta t}\|_{L^\infty(\mathcal{H}_{\Delta t})} \sum_{k=0}^{M-1} e^{kL\Delta t}.$$

342 The proof, based on the triangle inequality, follows that for Theorem 4.3 in Ref. 11. More-
 343 over, the gDMD is proven to have a tighter error bound than sDMD.⁹

344 Similarly, if \mathcal{L} is the xDMD, then the error $\delta_{\mathcal{L}}^M$ at time t_M satisfies the inequality

$$345 \quad \delta_{\mathcal{L}}^M \leq (1 + e^{L\Delta t})^M \delta_{\mathcal{L}}^0 + \|\mathcal{L} - \Phi_{\Delta t}\|_{L^\infty(\mathcal{H}_{\Delta t})} \sum_{k=0}^{M-1} (1 + e^{L\Delta t})^k.$$

346 The xDMD is proven to have a tighter error bound than rDMD.⁹ The error bounds provide
 347 a general guideline for the growth of errors.

348 Appendix B: Strategy to increase the xDMD efficiency

349 Direct evaluation of (9) requires the computation of $[\mathbf{B}_x \mathbf{b}_x] \in \mathbb{R}^{N \times N+1}$. Since N is large
 350 in any application of practical significance, this computation decreases the efficiency and
 351 accuracy of the algorithm. To avoid this bottleneck, we decompose the computation into
 352 two parts. First, we multiply only the first three terms of (9) thus leading to the matrix

$$353 \quad \mathbf{C}_x = \mathbf{Y} \mathbf{V}_g \boldsymbol{\Sigma}_g^{-1} \in \mathbb{R}^{N \times r}. \quad (\text{B1})$$

354 Second, we multiply the last term in (9) by $\tilde{\mathbf{x}}_k$, which gives a vector

$$355 \quad \mathbf{d}_x = \mathbf{U}_g^T \tilde{\mathbf{x}}_k \in \mathbb{R}^{r \times 1}. \quad (\text{B2})$$

356 This procedure leads to

$$357 \quad \mathbf{y}_{k+1} = \mathbf{C}_x \mathbf{d}_x, \quad (\text{B3})$$

358 which is equivalent to (8).

359 An overall step-by-step implementation of xDMD with the efficient computational strat-
 360 egy described in this Section, is illustrated in Algorithm 1.

Algorithm 1: xDMD implementation based on the efficient computational strategy.

1. Compute the residual matrix \mathbf{Y} : $\mathbf{Y} = \mathbf{X}' - \mathbf{X}$, where $\mathbf{Y} \in \mathbb{R}^{N \times M}$
 2. Introduce the matrix $\tilde{\mathbf{X}}$: $\tilde{\mathbf{X}}^\top = [\mathbf{X} \mathbf{1}]$, where $\tilde{\mathbf{X}}^\dagger \in \mathbb{R}^{N \times N+1}$
 3. Compute the truncated SVD of $\tilde{\mathbf{X}}$: $\tilde{\mathbf{X}} \approx \mathbf{U}_g \boldsymbol{\Sigma}_g \mathbf{V}_g^\top$, where $\mathbf{U}_g \in \mathbb{R}^{N+1 \times r}$, $\boldsymbol{\Sigma}_g \in \mathbb{R}^{r \times r}$, $\mathbf{V}_g \in \mathbb{R}^{M \times r}$
 4. Compute the matrix \mathbf{C}_x : $\mathbf{C}_x = \mathbf{Y} \mathbf{V}_g \boldsymbol{\Sigma}_g^{-1}$, where $\mathbf{C}_x \in \mathbb{R}^{N \times r}$
 5. Compute the vector \mathbf{d}_x : $\mathbf{d}_x = \mathbf{U}_g^\top \tilde{\mathbf{x}}_k$, where $\mathbf{d}_x \in \mathbb{R}^{r \times 1}$
 6. Compute the residual at $k+1$: $\mathbf{y}_{k+1} = \mathbf{C}_x \mathbf{d}_x$, where $\mathbf{y}_{k+1} \in \mathbb{R}^{N \times 1}$
 7. Compute the state at $k+1$: $\mathbf{x}_{k+1} = \mathbf{y}_{k+1} + \mathbf{x}_k$, where $\mathbf{x}_{k+1} \in \mathbb{R}^{N \times 1}$
-

REFERENCES

- ¹H. Lu and D. M. Tartakovsky, “Lagrangian dynamic mode decomposition for construction of reduced-order models of advection-dominated phenomena,” *Journal of Computational Physics* **407**, 109229 (2020).
- ²S. Dutta, M. W. Farthing, E. Perracchione, G. Savant, and M. Putti, “A greedy non-intrusive reduced order model for shallow water equations,” *Journal of Computational Physics* **439**, 110378 (2021).
- ³L. Pegolotti, M. R. Pfaller, A. L. Marsden, and S. Deparis, “Model order reduction of flow based on a modular geometrical approximation of blood vessels,” *Computer Methods in Applied Mechanics and Engineering* **380**, 113762 (2021).
- ⁴D. Colli, G. Libero, G. Pedrizzetti, and V. Ciriello, “Surrogate models provide new insights on metrics based on blood flow for the assessment of left ventricular function,” *Scientific Reports* **12** (2022), 10.1038/s41598-022-12560-3.
- ⁵A. Marzadri, V. Ciriello, and F. P. J. de Barros, “Hyporheic flows in stratified sediments: Implications on residence time distributions,” *Water Resources Research* **60**, e2023WR035625 (2024).
- ⁶V. Ciriello, I. Lauriola, S. Bonvicini, V. Cozzani, V. Di Federico, and D. M. Tartakovsky, “Impact of hydrogeological uncertainty on estimation of environmental risks posed by hydrocarbon transportation networks,” *Water Resources Research* **53**, 8686–8697 (2017).
- ⁷P. J. Schmid, “Dynamic mode decomposition of numerical and experimental data,” *Journal*

This is the author's peer reviewed, accepted manuscript. However, the online version of record will be different from this version once it has been copyedited and typeset.

PLEASE CITE THIS ARTICLE AS DOI: 10.1063/1.50207957

- 381 of Fluid Mechanics **656**, 5–28 (2010).
- 382 ⁸J. H. Tu, C. W. Rowley, D. M. Luchtenburg, S. L. Brunton, and J. N. Kutz, “On dynamic
383 mode decomposition: Theory and applications,” *Journal of Computational Dynamics* **1**,
384 391–421 (2014).
- 385 ⁹H. Lu and D. M. Tartakovsky, “Extended dynamic mode decomposition for inhomogeneous
386 problems,” *Journal of Computational Physics* **444**, 110550 (2021).
- 387 ¹⁰Z. Chen and D. Xiu, “On generalized residual network for deep learning of unknown
388 dynamical systems,” *Journal of Computational Physics* **438**, 110362 (2021).
- 389 ¹¹T. Qin, K. Wu, and D. Xiu, “Data driven governing equations approximation using deep
390 neural networks,” *Journal of Computational Physics* **395**, 620–635 (2019).
- 391 ¹²G. Libero, D. Tartakovsky, and V. Ciriello, “Polynomial chaos enhanced by dynamic mode
392 decomposition for order-reduction of dynamic models,” *Advances in Water Resources* **186**,
393 104677 (2024).
- 394 ¹³J. N. Kutz, S. L. Brunton, B. W. Brunton, and J. L. Proctor, *Dynamic Mode Decompo-*
395 *sition* (Society for Industrial and Applied Mathematics, 2016).
- 396 ¹⁴N. M. Wilson, A. K. Ortiz, and A. B. Johnson, “The vascular model repository: A public
397 resource of medical imaging data and blood flow simulation results,” *Journal of Medical*
398 *Devices* **7** (2013), 10.1115/1.4025983.
- 399 ¹⁵A. Updegrove, N. M. Wilson, J. Merkow, H. Lan, A. L. Marsden, and S. C. Shadden,
400 “SimVascular: An open source pipeline for cardiovascular simulation,” *Annals of Biomed-*
401 *ical Engineering* **45**, 525–541 (2016).
- 402 ¹⁶A. Arzani and S. T. M. Dawson, “Data-driven cardiovascular flow modelling: examples
403 and opportunities,” **18** (2021), 10.1098/rsif.2020.0802.
- 404 ¹⁷M. Habibi, S. T. M. Dawson, and A. Arzani, “Data-driven pulsatile blood flow physics
405 with dynamic mode decomposition,” **5**, 111 (2020).
- 406 ¹⁸Y. T. Delorme, A.-E. M. Kerlo, K. Anupindi, M. D. Rodefeld, and S. H. Frankel, “Dy-
407 namic mode decomposition of fontan hemodynamics in an idealized total cavopulmonary
408 connection,” **46**, 041425 (2014).
- 409 ¹⁹N. Groun, M. Villalba-Orero, E. Lara-Pezzi, E. Valero, J. Garicano-Mena, and
410 S. Le Clainche, “Higher order dynamic mode decomposition: From fluid dynamics to
411 heart disease analysis,” **144**, 105384 (2022).
- 412 ²⁰E. Ilicak, S. Ozdemir, J. Zapp, L. R. Schad, and F. G. Zöllner, “Dynamic mode decom-

This is the author's peer reviewed, accepted manuscript. However, the online version of record will be different from this version once it has been copyedited and typeset.

PLEASE CITE THIS ARTICLE AS DOI: 10.1063/1.50207957

- 413 position of dynamic MRI for assessment of pulmonary ventilation and perfusion,” **90**,
 414 761–769 (2023).
- 415 ²¹G. Di Labbio and L. Kadem, “Reduced-order modeling of left ventricular flow subject to
 416 aortic valve regurgitation,” **31** (2019), 10.1063/1.5083054.
- 417 ²²A. Stuart and A. R. Humphries, *Dynamical Systems and Numerical Analysis* (Cambridge
 418 University Press, 1998).
- 419 ²³H. Lu and D. M. Tartakovsky, “Prediction accuracy of dynamic mode decomposition,”
 420 SIAM Journal on Scientific Computing **42**, A1639–A1662 (2020).
- 421 ²⁴L. Pegolotti, M. R. Pfaller, N. L. Rubio, K. Ding, R. Brugarolas Brufau, E. Darve, and
 422 A. L. Marsden, “Learning reduced-order models for cardiovascular simulations with graph
 423 neural networks,” *Computers in Biology and Medicine* **168**, 107676 (2024).
- 424 ²⁵G. C. Bourantas, M. Ghommem, G. C. Kagadis, K. Katsanos, V. C. Loukopoulos, V. N.
 425 Burganos, and G. C. Nikiforidis, “Real-time tumor ablation simulation based on the
 426 dynamic mode decomposition method: Dynamic mode decomposition in tumor ablation
 427 simulation,” **41**, 053301 (2014).